Check for updates

Angewandte Chemie International Edition

Angewandte International Edition Chemie

How to cite: *Angew. Chem. Int. Ed.* **2026**, 65, e6865881
doi.org/10.1002/anie.6865881

RESEARCH ARTICLE

Implanted Zn^{2+}-Conducting Hydrogel Interphase Enables Highly Compacted Thick Iodine Electrodes for Ah-Level Aqueous Zinc–Iodine Pouch Batteries

Huadong Jiang | Chenxi Sun | Hong Lin | Minghao Zhang | Fanxiang Meng | Jinbao Zhao | Yang Yang

State Key Laboratory of Physical Chemistry of Solid Surfaces, State-Province Joint Engineering Laboratory of Power Source Technology for New Energy Vehicle, College of Chemistry and Chemical Engineering, Xiamen University, Xiamen, P. R. China

Correspondence: Jinbao Zhao (jbzhao@xmu.edu.cn) | Yang Yang (yangyang419@xmu.edu.cn)

Received: 19 May 2026 | **Revised:** 29 July 2026 | **Accepted:** 3 August 2026

Keywords: aqueous zinc–iodine batteries | highly compacted dry-processed electrodes | PAMPS-Zn hydrogel interphase | polyiodide shuttling suppression | Zn^{2+}-conducting hydrogel

ABSTRACT

Increasing the compaction density of dry-processed thick iodine cathodes is essential for enhancing energy density, yet remains hindered by sluggish reaction kinetics and aggravated polyiodide shuttling. Herein, we report an implanted Zn^{2+}-conducting (PAMPS-Zn, poly(zinc 2-acrylamido-2-methylpropane sulfonate)) hydrogel interphase via in situ ultraviolet-induced polymerization, which enables local Zn^{2+} buffering, enhanced Zn^{2+} transport, and suppression of polyiodide migration in highly compacted dry-processed iodine cathodes. Abundant sulfonate groups in polymeric chains serve as immobilized anionic sites that coordinate Zn^{2+} and provide a local Zn^{2+} reservoir, which mitigates interfacial Zn^{2+} depletion. Meanwhile, the interconnected Zn^{2+}-conducting hydrogel network facilitates Zn^{2+} transport through the thick electrode, reducing reliance on conventional electrolyte-permeation-mediated ion transport in dry-processed electrodes, which is intrinsically limited by the hydrophobic nature of the PTFE binder and high ionic tortuosity. Importantly, the negatively charged, water-regulated hydrogel interphase also suppresses polyiodide diffusion through electrostatic repulsion and reduced water-driven dissolution. Consequently, under high compaction conditions (~0.5 g cm^{-3}), Zn–I_2 batteries incorporating PAMPS-Zn interphase achieve a high areal capacity of 9.6 mAh cm^{-2} at 0.5 C and an ultralong lifespan exceeding 4400 cycles at 5 C. Notably, Ah-level Zn-I_2 pouch cells (~1.2 Ah) achieve stable operation for 850 cycles, providing compelling proof-of-concept validation of this strategy.

1 | Introduction

Driven by the growing demand for safe and cost-effective battery technologies for large-scale energy storage, aqueous zinc–iodine (Zn–I_2) batteries have emerged as a promising complement to existing lithium-ion batteries (LIBs) owing to the high theoretical capacity (211 mAh g^{-1} based on I^-/I^0 redox couple), their considerable output voltage (~1.3 V vs. Zn^{2+}/Zn), and the natural abundance of iodine resources (55 μg L^{-1} in seawater) [1–10]. Laboratory-scale Zn–I_2 batteries have achieved stable operation for more than 10,000 cycles [7, 11–16]. However, their practical deployment still remains limited because most reported systems rely on low-loading, wet-processed cathodes in coin-cell configurations, which severely restrict the areal capacity (<3 mAh cm^{-2}) [8, 16–20]. Recently, dry-processed iodine cathodes have shown promise for high-areal-capacity applications [21, 22], and our

Huadong Jiang and Chenxi Sun contributed equally to this work.

All rights reserved, including rights for text and data mining and training of artificial intelligence technologies or similar technologies.
© 2026 Wiley-VCH GmbH

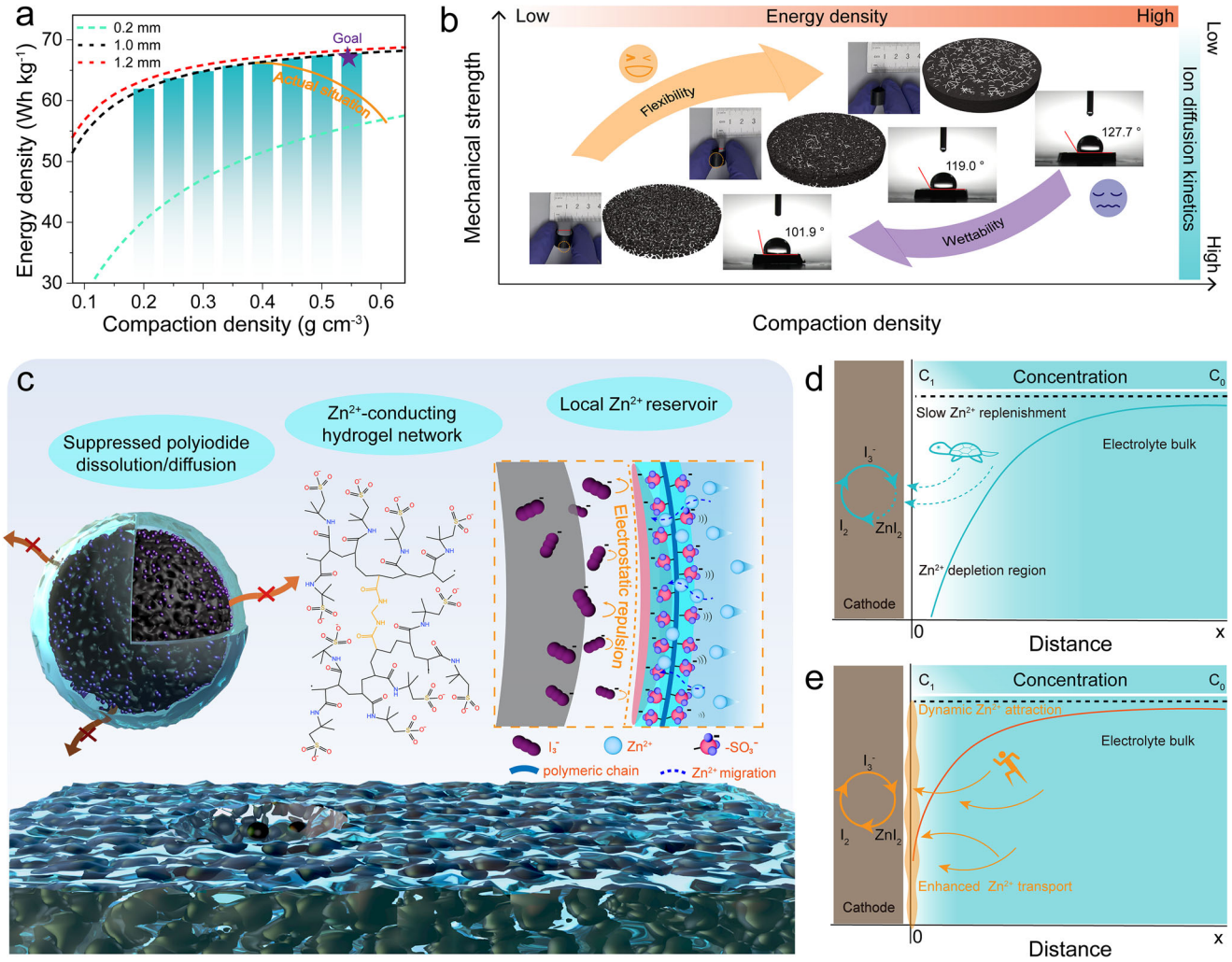

FIGURE 1 | Design of the PAMPS-Zn interphase for highly compacted dry-processed iodine cathodes. (a) Dependence of energy density on the compaction density of dry-processed iodine cathodes. (b) Schematic illustration of the fibrillated PTFE network formed during repeated rolling and the associated increase in mechanical strength together with deteriorated electrolyte wettability. (c) Schematic illustration of the proposed strategy for introducing a Zn^{2+}-conducting PAMPS-Zn hydrogel into highly compacted dry-processed thick electrodes through precursor infiltration and ultraviolet-induced in situ polymerization. (d) Schematic illustration of the Zn^{2+} depletion effect at the cathode interface in highly compacted thick electrodes during discharge. (e) Schematic illustration of the charge-balanced PAMPS-Zn interphase, highlighting the proposed local Zn^{2+} reservoir and facilitated Zn^{2+} transport mechanism.

group further demonstrated their compatibility with continuous roll-to-roll manufacturing [23]. For dry-processed electrodes, areal capacity is governed primarily by electrode thickness and compaction density (Equation S1). However, further increasing electrode thickness (>1 mm) yields diminishing marginal gains in device-level energy density (Figures 1a and S1), whereas increasing compaction density more effectively enhances both energy density and space-utilization efficiency [24–27]. Experiences from commercial $LiFePO_4$ cathode materials for LIBs also indicate that thick, highly compact electrodes represent an inevitable path toward the practical battery deployment [28–30].

During dry processing, increasing the calendaring pressure and rolling frequency can effectively enhance the compaction density, but it also causes a pronounced deterioration in ionic-transport kinetics within compacted thick electrodes [24, 29, 31, 32]. For iodine cathodes, the achievable compaction density exhibits a clear upper limit, beyond which a rapid decline in specific-capacity delivery is observed. First, high compaction reduces electrode porosity, increases tortuosity, and prolongs ion-transport pathways, while the shrinkage of internal voids induces capillary effects that further hinder electrolyte infiltration. Meanwhile, repeated rolling triggers excessive fibrillation of the intrinsically hydrophobic PTFE binder, which improves electrode robustness but further impedes electrolyte penetration.

Another often overlooked kinetic limitation for high-areal-capacity iodine cathodes lies in the ion-supply efficiency [33, 34]. During discharge, the conversion of I_2 into ZnI_2 in the electrode requires continuous and abundant uptake of Zn^{2+} from the electrolyte. Notably, the complete conversion of a high-areal-capacity dry-processed iodine cathode delivering 10 mAh cm^{-2} requires approximately 186.6 μmol cm^{-2} of Zn^{2+}, which exceeds the Zn^{2+} inventory supplied by 100 μL of 2 M $ZnSO_4$ electrolyte when normalized to the cathode area (ca. 176.8 μmol cm^{-2}). Rapid Zn^{2+} consumption at the cathode/electrolyte interface,

15213773, 2026, 42, Downloaded from https://onlinelibrary.wiley.com/doi/10.1002/anie.6865881 by Xiamen University, Wiley Online Library on [19/11/2026]. See the Terms and Conditions (https://onlinelibrary.wiley.com/terms-and-conditions) on Wiley Online Library for rules of use; OA articles are governed by the applicable Creative Commons License

together with the opposite migration of SO_4^{2-} under the internal electric field, generates a pronounced concentration gradient resembling a space-charge layer region (Figure 1d), thereby impeding Zn^{2+} replenishment from the electrolyte into the bulk electrode [33, 35–38]. Under such conditions, maintaining local Zn^{2+} availability requires not only sufficient ionic conductivity, but also continuous transport from the bulk electrolyte toward internal reaction regions. Moreover, high iodine loading also inevitably aggravates the polyiodide shuttle effect, resulting in self-discharge and active-material loss [11, 16, 39–42]. Although many strategies, including carbon-host modification, electrolyte regulation and functional-separator design, have been developed to suppress polyiodide shuttling, their effectiveness under high-areal-capacity conditions still requires further evaluation. Importantly, the critical process of water-induced polyiodide dissolution/diffusion has rarely been explicitly addressed in these strategies [43–47]. Therefore, developing high-compaction-density thick iodine electrodes with fast reaction kinetics and suppressed polyiodide shuttling remains highly challenging.

In this work, a Zn^{2+}-conducting PAMPS-Zn (poly(zinc 2-acrylamido-2-methylpropane sulfonate)) hydrogel interphase is implanted into highly compacted thick iodine electrodes, providing local Zn^{2+} buffering, facilitating Zn^{2+} transport, and suppressing polyiodide dissolution/diffusion (Figure 1c). The AMPS-Zn precursor solution completely infiltrates the compact iodine electrode and undergoes ultraviolet-induced in situ polymerization, forming an implanted PAMPS-Zn hydrogel network throughout the electrode. The immobilized sulfonate ($-SO_3^-$) groups on the polymeric chains act as fixed anionic sites that coordinate Zn^{2+} and provide a local Zn^{2+} reservoir. Meanwhile, the interconnected hydrogel network establishes Zn^{2+}-conducting pathways that facilitate Zn^{2+} transport from the bulk electrolyte toward internal reaction regions (Figure 1e). This combined function facilitates Zn^{2+} transport within the compact electrode despite limited electrolyte infiltration. Importantly, the negatively charged hydrogel interphase distributed throughout the electrode suppresses polyiodide shuttling through the combined effects of electrostatic repulsion and reduced water-driven dissolution. Consequently, the modified cathode mitigates the kinetic limitations associated with highly compacted dry-processed iodine electrodes, delivering a high areal capacity of 9.6 mAh cm^{-2} at 0.5 C and a cycling life exceeding 4400 cycles at a high compaction density of ~0.5 g cm^{-3}, corresponding to an approximately 19% increase in cathode compaction density compared with the conventional value of ~0.419 g cm^{-3}. More importantly, this strategy can be integrated into dry-processed electrode manufacturing lines for the fabrication of Ah-level pouch cells, indicating its potential compatibility with scalable production.

2 | Results and Discussion

2.1 | Implantation of PAMPS-Zn Hydrogel in Highly Compacted I_2 Electrodes

To clarify the structural consequences of high compaction and verify the feasibility of in situ hydrogel construction, a series of thick dry-processed electrodes (~47 mg cm^{-2}) with compaction densities ranging from 0.419 to 0.511 g cm^{-3} were prepared by repeated rolling (the compaction density was calculated based on the mass density of active material iodine; Table S1). Increasing the compaction density markedly improves the mechanical strength of the dry-processed electrodes, as reflected by increases in maximum tensile stress from 0.07 to 0.42 MPa and the tensile strain to 17.1% (Figure 2a). This enhancement is attributed to the more extensive PTFE fibrillation network generated under shear force during rolling [21, 23]. Moreover, the reduced interparticle distance under high compaction pressure further reinforces the structural integrity of the electrode and the electronically conductive network formed by Super P and Ketjen black. Consistently, structural densification increases the electronic conductivity from 0.26 to 0.40 S cm^{-1}, corresponding to a 53.8% enhancement (Figure 2b). However, these mechanical and electronic gains are accompanied by deteriorated electrolyte wettability: the contact angle increases from 101.9° to 127.7° (insets in Figure 1b), suggesting increasingly hindered electrolyte infiltration. As shown in Figure 2c, the initial specific capacity and maximum tensile stress exhibit a clear trade-off with increasing compaction density. At low compaction density, the electrode delivers a specific capacity of 202 mAh g^{-1}, close to the theoretical capacity of iodine (211 mAh g^{-1}). Incomplete capacity utilization emerges once the compaction density approaches 0.46 g cm^{-3} and becomes severe at 0.511 g cm^{-3}, where the specific capacity falls below 50 mAh g^{-1}, corresponding to only 23.7% theoretical utilization. This severe capacity loss indicates that ionic transport becomes strongly hindered in the highly compacted electrode, thereby motivating the construction of an internal ion-conducting phase via in situ hydrogel polymerization (Figures S2 and S3) [48, 49].

Spectroscopic analyses were then performed to verify both the successful polymerization of PAMPS-Zn and its introduction into the highly compacted electrode. In the Fourier-transform infrared (FTIR) spectroscopy (Figure 2d), the AMPS monomer exhibits a characteristic vinyl vibration near 1610 cm^{-1}, which markedly weakens after polymerization, whereas the characteristic $-SO_3^-$ peaks at 1040 and 1200 cm^{-1} are retained together with the amide vibration around 1650 cm^{-1}, consistent with the formation of PAMPS-Zn [50, 51]. After hydrogel implantation, the gel-implanted dry-processed cathode (GEL-DC) exhibits the characteristic PAMPS-Zn bands absent from the pristine dry-processed cathode (DC), and Raman spectra further show the C-H vibration of PAMPS-Zn at 2800–3000 cm^{-1} together with substantial overlap with the pure hydrogel in the 600–1800 cm^{-1} fingerprint region (Figure 2e). These features confirm that the hydrogel phase is introduced into the electrode and establishes intimate contact with the activated-carbon framework. To further evaluate the penetration depth and through-thickness uniformity of the in situ polymerization strategy in ultrathick dry-processed electrodes, cross-sectional scanning electron microscopy (SEM) and energy-dispersive x-ray spectroscopy (EDS) elemental mapping were performed on GEL-DC (Figure 2f). The cross-sectional SEM images confirm the densely packed 1 mm-thick electrode architecture, while EDS mapping shows homogeneous carbon and iodine distribution across the electrode thickness. More importantly, the continuous sulfur distribution, originating from the sulfonate groups of PAMPS-Zn, demonstrates complete precursor penetration and through-thickness hydrogel formation after photopolymerization.

15213773, 2026, 42, Downloaded from https://onlinelibrary.wiley.com/doi/10.1002/anie.6865881 by Xiamen University, Wiley Online Library on [19/11/2026]. See the Terms and Conditions (https://onlinelibrary.wiley.com/terms-and-conditions) on Wiley Online Library for rules of use; OA articles are governed by the applicable Creative Commons License

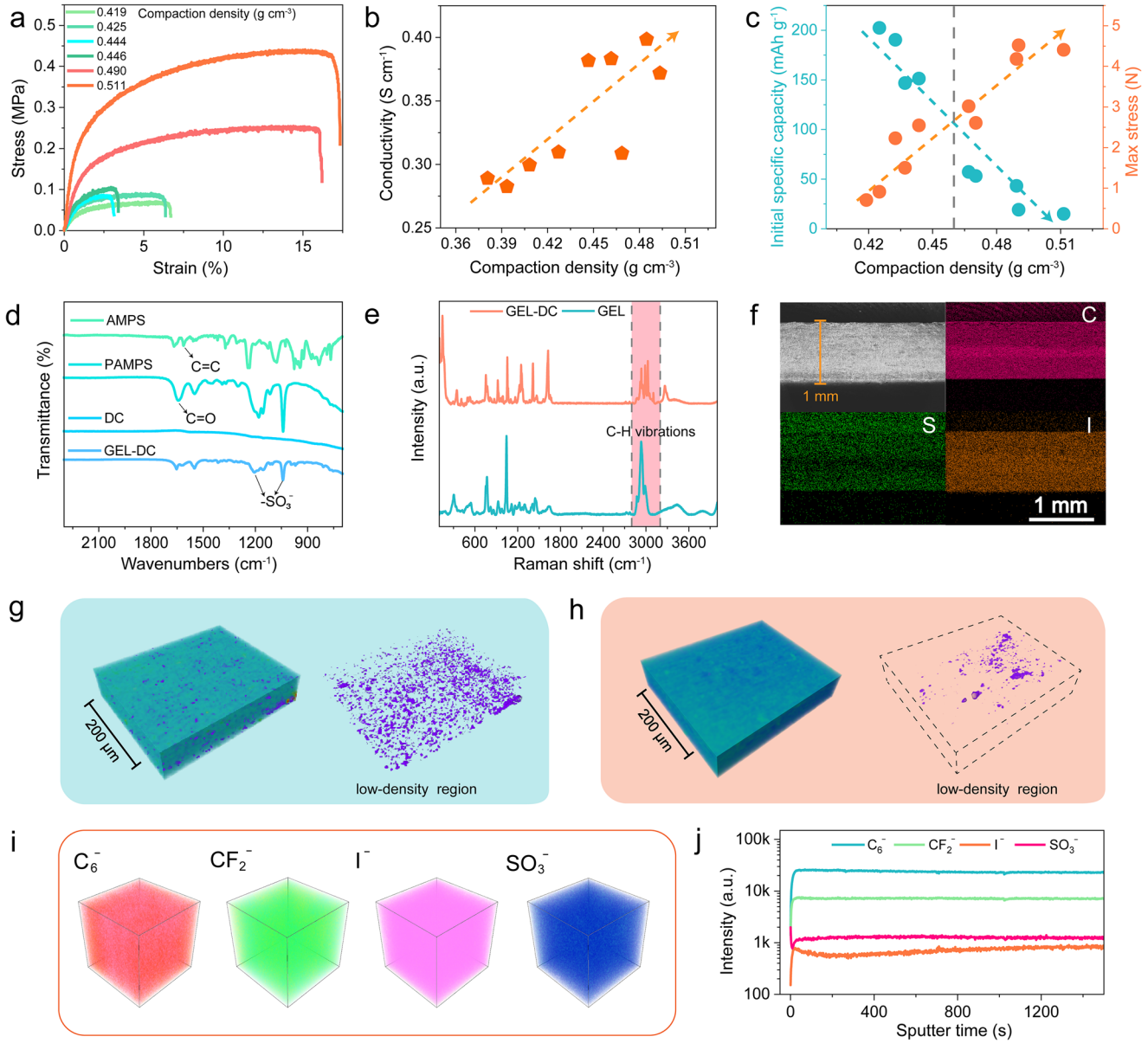

FIGURE 2 | Implantation of PAMPS-Zn hydrogel in highly compacted I_2 electrodes. (a) Stress-strain curves of dry-processed electrodes with different compaction densities. (b) Electronic conductivity of dry-processed electrodes as a function of compaction density. (c) Initial specific capacity and maximum tensile stress of dry-processed electrodes with different compaction densities. (d) FTIR spectra of the AMPS monomer, PAMPS-Zn gel, pristine dry-processed cathode (DC), and gel-modified dry-processed cathode (GEL-DC). (e) Raman spectra of the PAMPS-Zn gel, DC, and GEL-DC. (f) Cross-sectional SEM images and corresponding EDS elemental maps of GEL-DC. (g) Three-dimensional micro-CT reconstruction of DC, highlighting the residual internal pores in the highly compacted electrode. (h) Three-dimensional micro-CT reconstruction of GEL-DC, showing that the PAMPS-Zn gel fills the microscopic voids and establishes a continuous three-dimensional ion-conducting network. (i) TOF-SIMS three-dimensional distribution of characteristic ionic fragments in GEL-DC. (j) Depth profiling of the characteristic ionic fragments in GEL-DC.

Three-dimensional micro-computed tomography (3D-CT) was further employed to visualize the internal density distribution and pore configuration of the highly compacted electrodes. After 3D reconstruction, the extracted low-signal regions reveal residual internal voids in DC (Figure 2g), which are difficult to be completely wetted by the aqueous electrolyte due to the hydrophobic nature of PTFE nanofibers. By contrast, after PAMPS-Zn introduction, these low-signal void regions are largely diminished (Figure 2h), indicating that the hydrogel effectively infiltrates the microscopic interparticle voids to form a more continuous three-dimensional ion-conducting network. Further TOF-SIMS (time-of-flight secondary ion mass spectrometry) analysis provides spatially and depth-resolved evidence for the PAMPS-Zn phase in GEL-DC. The three-dimensional ion maps reveal that I^- and I_2^- closely overlap with the carbon-framework signal C_6^- and the binder-derived signal CF_2^-, consistent with a homogeneous iodine-loaded carbon matrix (Figure 2i). PAMPS-Zn-related fragments, represented here by SO_3^-, $CH_2SO_3^-$, $C_4H_8SO_3^-$, and ZnO^- (Figure S4), show the same spatial trend. The corresponding depth profiles show sustained signal intensities with increasing sputtering time, further confirming the formation of a continuous PAMPS-Zn phase throughout the

15213773, 2026, 42, Downloaded from https://onlinelibrary.wiley.com/doi/10.1002/anie.6865881 by Xiamen University, Wiley Online Library on [19/11/2026]. See the Terms and Conditions (https://onlinelibrary.wiley.com/terms-and-conditions) on Wiley Online Library for rules of use; OA articles are governed by the applicable Creative Commons License

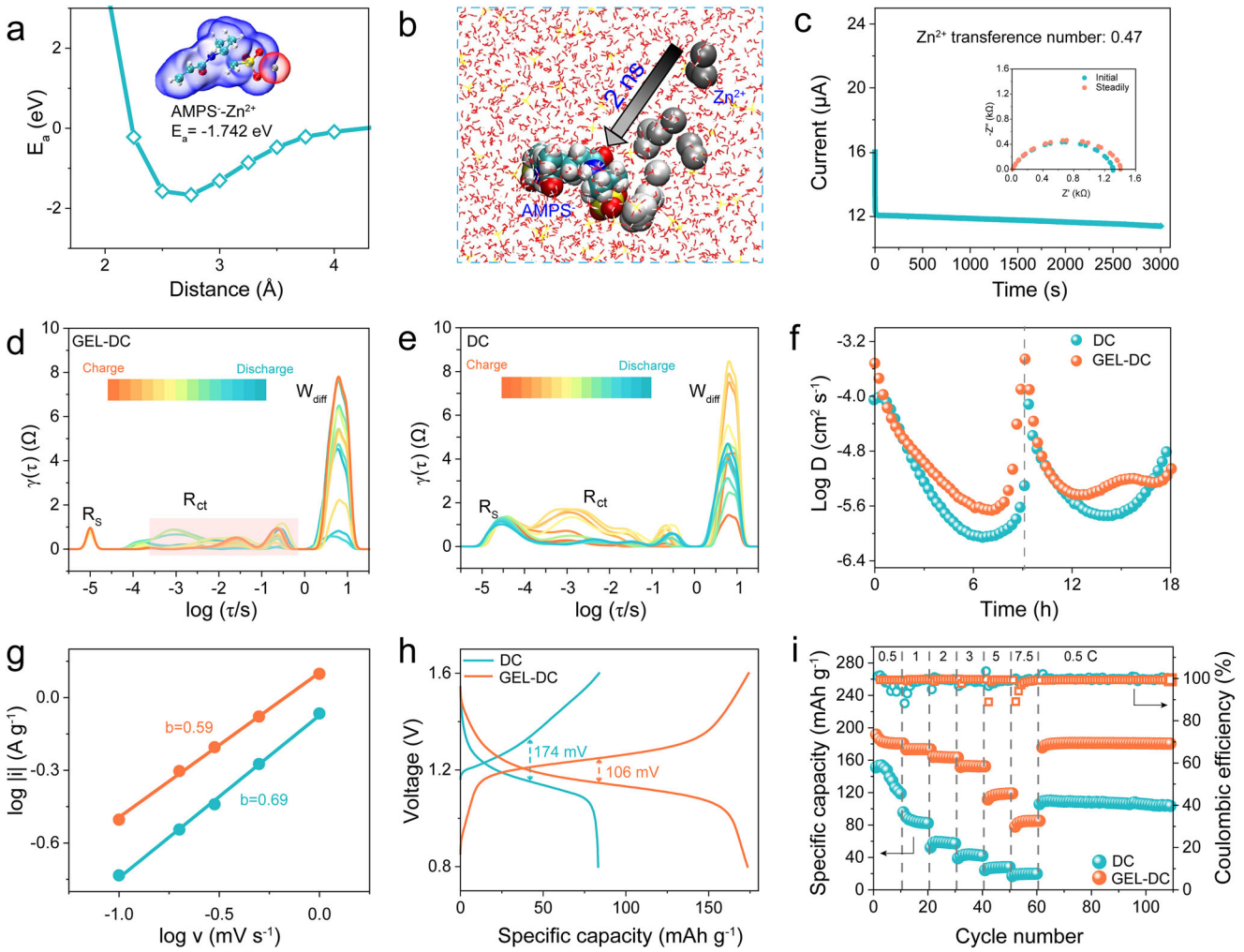

FIGURE 3 | Rapid ion transport paths via the implanted PAMPS-Zn hydrogel network. (a) Calculated interaction energy between the $AMPS^-$ site and Zn^{2+} as a function of distance. (b) Molecular dynamics snapshots showing the approach of Zn^{2+} toward the $AMPS^-$ site with increasing simulation time. (c) Zn^{2+} transference number measured in a Zn||Zn symmetric cell using 1 M PAMPS-Zn gel as the electrolyte. (d) DRT analysis of in situ EIS for Zn||GEL-DC at different charge/discharge states. (e) DRT analysis of in situ EIS for Zn||DC at different charge/discharge states. (f) Zn^{2+} diffusion coefficients derived from GITT for Zn||DC and Zn||GEL-DC during charge and discharge. (g) *b*-value analysis based on scan-rate-dependent cyclic voltammetry for Zn||DC and Zn||GEL-DC. (h) Galvanostatic charge-discharge curves of Zn||DC and Zn||GEL-DC. (i) Rate performance and corresponding Coulombic efficiency of Zn||DC and Zn||GEL-DC over a wide current-rate range.

compact electrode (Figure 2j). Notably, the implantation of PAMPS-Zn hydrogel preserves the tensile behavior of the highly compacted cathode, with a slight increase in maximum tensile stress, while maintaining comparable electronic conductivity and causing only a ~1.6% increase in electrode thickness (Figure S5).

2.2 | Rapid Ion Transport Paths via the Implanted PAMPS-Zn Hydrogel Network

The implanted PAMPS-Zn hydrogel is expected to provide interconnected Zn^{2+}-transport pathways in highly compacted dry-processed electrodes, thereby facilitating Zn^{2+} penetration into the electrode interior and improving the overall reaction kinetics. The calculated interaction profile shows a pronounced energy well between the $AMPS^-$ site and Zn^{2+}, with the energy minimum appearing at approximately 2.7 Å and an interaction energy of −1.742 eV (Figure 3a) [52]. This favorable interaction supports the role of the $-SO_3^-$ groups in the hydrogel framework as Zn^{2+}-coordination sites. Molecular dynamics (MD) simulations further visualize this attraction-driven process, as a single Zn^{2+} ion initially located away from $AMPS^-$ gradually approaches the $AMPS^-$ site within 2 ns (Figure 3b). Consistent with this molecular affinity, the Zn^{2+} transference number of the PAMPS-Zn hydrogel electrolyte reaches 0.47 in a Zn||Zn symmetric cell, markedly higher than that of the liquid electrolyte (0.24; Figures 3c and S6). The moderate Zn^{2+} transference number is attributed to the local swing of the polyanionic chains [51]. The PAMPS-Zn hydrogel also exhibits an ionic conductivity of 31.6 mS cm^{-1}, comparable to that of the similarly ion-conducting poly(sodium 2-acrylamido-2-methylpropane sulfonate) (PAMPS-Na) hydrogel, whereas the non-ion-conducting polyacrylamide (PAAm) hydrogel shows a much lower value of only 0.013 mS cm^{-1}. Although its ionic conductivity is lower than that of the 2 M $ZnSO_4$-soaked glass fiber (GF/D) separator (44.6 mS cm^{-1}), the key advantage of PAMPS-Zn lies in spatially

15213773, 2026, 42, Downloaded from https://onlinelibrary.wiley.com/doi/10.1002/anie.6865881 by Xiamen University, Wiley Online Library on [19/11/2026]. See the Terms and Conditions (https://onlinelibrary.wiley.com/terms-and-conditions) on Wiley Online Library for rules of use; OA articles are governed by the applicable Creative Commons License

integrating Zn^{2+}-conducting pathways into the highly compacted cathode (Figure S7). Quantitative uptake analysis shows that the implanted PAMPS-Zn phase provides an areal Zn^{2+} inventory of approximately 21.1 μmol cm^{-2}, corresponding to ~11% of the areal Zn^{2+} demand of 186.6 μmol cm^{-2} for complete discharge of a cathode delivering 10 mAh cm^{-2}. Thus, the hydrogel provides a local Zn^{2+} reservoir while facilitating Zn^{2+} transport through the compact electrode. The Zn||Zn symmetric cell using PAMPS-Zn hydrogel sustains reversible Zn plating/stripping for 200 h, supporting Zn^{2+} conduction through the hydrogel during repeated electrochemical operation (Figure S13d). To investigate the effect of PAMPS-Zn under kinetically constrained high-compaction-density conditions, the following electrochemical studies were conducted using dry-processed cathodes with high compaction densities of 0.48–0.50 g cm^{-3}. In situ EIS (electrochemical impedance spectroscopy) coupled with DRT (distribution of relaxation times) analysis further links this molecular-level Zn^{2+} regulation to improved interfacial reaction kinetics (Figures 3d,e, and S8) [39, 53]. Compared with Zn||DC, Zn||GEL-DC exhibits a markedly reduced R_{ct} throughout the charge/discharge process, with R_{ct} varying within 0.091–0.884 Ω for Zn||GEL-DC, compared with 0.204–1.710 Ω for Zn||DC. This lower R_{ct} reflects facilitated interfacial charge transfer and faster iodine conversion kinetics in the highly compacted cathode. Meanwhile, the lower and more stable W_{diff} response of GEL-DC suggests mitigated Zn^{2+} diffusion limitation. These results correlate the Zn^{2+}-coordination capability of PAMPS-Zn with reduced interfacial resistance and accelerated reaction kinetics in highly compacted dry-processed I_2 cathodes.

The Zn^{2+} diffusion coefficients derived from GITT (galvanostatic intermittent titration technique) analysis further support this conclusion (Figure 3f). During discharge, both electrodes show a gradual decrease in Zn^{2+} diffusivity as the reaction proceeds, yet Zn||GEL-DC maintains higher values throughout most of the process. Its diffusion coefficient is 3.03×10^{-4} cm^2 s^{-1} at the beginning of discharge, higher than that of Zn||DC (8.30×10^{-5} cm^2 s^{-1}), and remains higher near the end of discharge (2.41×10^{-6} cm^2 s^{-1} vs. 9.29×10^{-7} cm^2 s^{-1}), indicating mitigated diffusional deterioration. Upon subsequent charging, Zn||GEL-DC exhibits a much faster recovery, reaching 3.48×10^{-4} cm^2 s^{-1} at the beginning of charge, whereas Zn||DC remains much lower (Equation S2). Thus, the PAMPS-Zn gel mitigates discharge-induced transport deterioration and enables rapid kinetic recovery during charge. Scan-rate-dependent cyclic voltammetry measurements reveal a consistent trend (Figure S9). The *b*-values of Zn||DC and Zn||GEL-DC are 0.69 and 0.59, respectively (Figure 3g). Although both values lie between 0.5 and 1.0, indicating mixed diffusion-controlled and surface-capacitive contributions, the lower b-value of Zn||GEL-DC suggests a larger diffusion-controlled contribution. Together with the higher current response and faster Zn^{2+} diffusion revealed by GITT, this behavior indicates that the implanted hydrogel enables deeper redox utilization within the electrode interior rather than limiting the reaction to near-surface regions.

The improved transport kinetics translate directly into superior rate performance (Figures 3 h,i, S10, and S11). At 0.5 C, Zn||GEL-DC delivers 191.65 mAh g^{-1}, corresponding to a high areal capacity of 9.6 mAh cm^{-2}, whereas Zn||DC delivers only 118.86 mAh g^{-1}. As the current rate increases from 1 to 2, 3, 5, and 7.5 C, Zn||GEL-DC still maintains high specific capacities of 173.41, 163.20, 152.34, 118.87, and 85.10 mAh g^{-1}, respectively. By contrast, the capacity decay of Zn||DC becomes much more pronounced, retaining only 82.16, 57.11, 42.11, 27.90, and 19.87 mAh g^{-1} at the corresponding rates. The galvanostatic profiles further show flatter voltage plateaus and reduced polarization for Zn||GEL-DC across the tested rate range, with the voltage hysteresis at 1 C decreasing from 174 mV for Zn||DC to 106 mV (Figure 3h). When the current rate is switched back to 0.5 C, Zn||GEL-DC rapidly recovers to 181.15 mAh g^{-1} and remains stable, whereas Zn||DC recovers only to 108.76 mAh g^{-1} and further decays to 103.40 mAh g^{-1}. These results demonstrate that the implanted PAMPS-Zn phase effectively preserves ion accessibility within the compact electrode, thereby sustaining high iodine utilization and fast reaction kinetics under elevated current rates [21, 39]. Consistently, ultraviolet–visible (UV–vis) spectroscopy analysis of the fully discharged electrodes confirms more complete iodine utilization in GEL-DC, as evidenced by the weaker residual iodine signal and the substantially lower amount of extracted unreacted iodine compared with DC (Figure S12).

2.3 | Suppression of Polyiodide Dissolution/Diffusion

In addition to Zn^{2+} transport, the spatial distribution and migration behavior of iodine species near the interface exert a profound influence on the reversibility of Zn–I_2 batteries. Soluble polyiodide anions can diffuse away from the cathode, causing active-material loss and interfacial side reactions. Therefore, an effective interphase is expected to support rapid Zn^{2+} transport while selectively regulating iodine-containing anions. As shown in Figure 4a, the interaction profile between $AMPS^-$ and I_3^- exhibits a clear repulsive trend. As the distance decreases, the interaction rapidly becomes unfavorable, revealing increasingly strong electrostatic repulsion between the sulfonate groups and polyiodide species. MD simulations were further performed to visualize this repulsion effect more directly. Whereas I_3^- remains dispersed in the electrolyte in the absence of $AMPS^-$ (Figure 4b), nearby I_3^- species spontaneously move away from the $AMPS^-$ region within 2 ns after $AMPS^-$ is introduced (Figure 4c), supporting the electrostatic repulsion between $AMPS^-$ and I_3^-. The negatively charged polymerized PAMPS-Zn layer hinders the cross-interfacial migration of polyiodides, thereby reducing their outward diffusion from the electrode into the electrolyte (Figure 4d). Control experiments using PAAm and PAMPS-Na hydrogels further clarify the role of the fixed sulfonate framework in suppressing polyiodide migration. The nonionic PAAm hydrogel exhibits pronounced polyiodide diffusion, whereas PAMPS-Na, which retains the fixed sulfonate framework, substantially suppresses polyiodide transport (Figures S13a–c).

In situ optical microscopy was further employed to directly visualize the macroscopic suppression of iodine-species dissolution. Bare Pt wire and PAMPS-Zn hydrogel coated Pt wire were immersed in ZnI_2 electrolyte and charged to continuously generate I_2 on the Pt surface, which subsequently complexes with I^- in the solution to form I_3^-. The dissolution and outward diffusion of I_3^- were monitored by the color evolution of the surrounding electrolyte. The voltage-time curves of the two systems are nearly identical (Figure S14), confirming that

15213773, 2026, 42, Downloaded from https://onlinelibrary.wiley.com/doi/10.1002/anie.6865881 by Xiamen University, Wiley Online Library on [19/11/2026]. See the Terms and Conditions (https://onlinelibrary.wiley.com/terms-and-conditions) on Wiley Online Library for rules of use; OA articles are governed by the applicable Creative Commons License

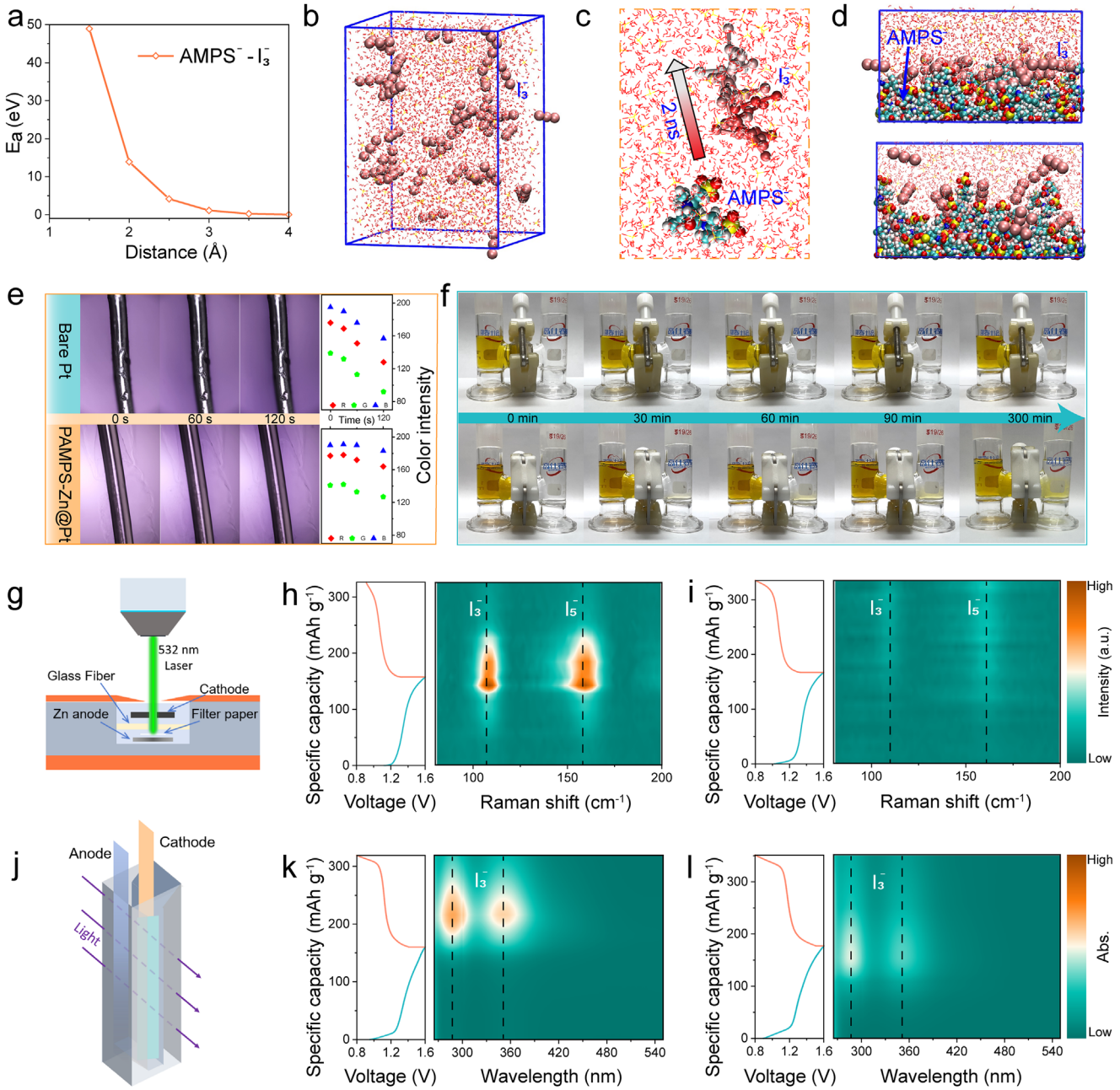

FIGURE 4 | Suppression of polyiodide dissolution/diffusion. (a) Calculated interaction profile between $AMPS^-$ and I_3^- as a function of distance. (b) Molecular dynamics snapshot showing the dispersed distribution of I_3^- in the electrolyte in the absence of $AMPS^-$. (c) Molecular dynamics snapshot showing that I_3^- is repelled away from the $AMPS^-$ region with increasing simulation time. (d) Molecular dynamics model of the polymerized PAMPS-Zn framework. (e) In situ optical microscopy images of bare Pt and PAMPS-Zn-coated Pt during polarization in ZnI_2 electrolyte, together with the corresponding RGB intensity evolution, visualizing the dissolution behavior of I_3^- near the electrode surface. (f) H-cell diffusion test using gel-containing glass fiber and bare glass fiber as the separator. (g) Schematic illustration of the in situ Raman measurement setup. (h) In situ Raman spectra of the electrolyte in the cell using DC as the cathode. (i) In situ Raman spectra of the electrolyte in the cell using GEL-DC as the cathode. (j) Schematic illustration of the in situ UV–vis measurement setup. (k) In situ UV–vis spectra of the electrolyte in the cell using DC as the cathode. (l) In situ UV–vis spectra of the electrolyte in the cell using GEL-DC as the cathode.

comparable amounts of iodine species are generated at these two reaction interfaces. However, as revealed by the in situ optical micrographs and the RGB intensity evolution at the same local position (Figure 4e), the electrolyte surrounding the bare Pt wire exhibits an obvious dark region associated with the generation and outward diffusion of I_3^-, accompanied by a rapid change in RGB intensity. In contrast, the electrolyte near the hydrogel-coated Pt wire remains bright, and the RGB intensity remains nearly unchanged. The I_3^- diffusion experiments were also carried out in a macroscopic H-cell separated by either bare GF or hydrogel-containing GF. The deionized-water side remains colorless and transparent even after 300 min when the hydrogel-containing separator is used, whereas visible yellowing appears within 60 min with bare glass fiber, demonstrating constrained

15213773, 2026, 42, Downloaded from https://onlinelibrary.wiley.com/doi/10.1002/anie.6865881 by Xiamen University, Wiley Online Library on [19/11/2026]. See the Terms and Conditions (https://onlinelibrary.wiley.com/terms-and-conditions) on Wiley Online Library for rules of use; OA articles are governed by the applicable Creative Commons License

polyiodide diffusion through the hydrogel-containing separator (Figure 4f).

In situ spectroscopic measurements further reveal the suppression of the shuttle effect by PAMPS-Zn under realistic battery operating conditions [7, 54, 55]. In the cell using DC as the cathode, distinct signals appear near 110 and 160 cm^{-1} during a charge/discharge cycle, which can be assigned to I_3^- and I_5^- species, respectively, and persist throughout the entire process (Figures 4g,h). This result indicates that soluble polyiodide species continuously dissolve from the cathode and diffuse across the separator toward the Zn side. By contrast, in the cell assembled with GEL-DC, the Raman responses in the 110 and 160 cm^{-1} regions are reduced by 73.9% and 55.0%, respectively (Figure 4i), evidencing effective suppression of the outward diffusion and shuttling of polyiodide species toward the anode. In situ UV–vis spectroscopy provides complementary evidence using a quartz-cuvette cell with the dry-processed cathode and Zn foil attached to opposite sides (Figure 4j). In the untreated DC system, strong absorption responses appear near 290 and 360 nm (Figure 4k), reflecting substantial release of polyiodide species during cycling. In contrast, the corresponding absorption peaks are markedly attenuated in GEL-DC (Figure 4l), indicating that the amount of polyiodide anions entering the bulk electrolyte is greatly reduced [54–56]. Consistently, the self-discharge test shows that Zn||GEL-DC retains 97.9% of its capacity after a 24 h rest, much higher than that of Zn||DC, further supporting the inhibited polyiodide shuttling behavior (Figure S15). Together, these in situ results demonstrate the effective suppression of polyiodide migration during battery operation.

2.4 | Device-Level Proof-of-Concept Validation and Fabrication Compatibility

Based on the dual role of PAMPS-Zn in promoting Zn^{2+} transport and suppressing polyiodide migration, we next evaluated whether this mechanism translates into durable electrochemical performance in large-area pouch and cylindrical cell formats. In long-term cycling tests of coin cells at 5 C using dry-processed cathodes with a compaction density of 0.502 g cm^{-3}, the Zn||GEL-DC cell exhibits significantly superior stability compared with Zn||DC (Figure 5a). After initial activation, the Zn||GEL-DC cell delivers a discharge capacity of 5.92 mAh cm^{-2} (117.93 mAh g^{-1}) and still maintains 5.03 mAh cm^{-2} (99.97 mAh g^{-1}) at the 4000th cycle, corresponding to 84.9% capacity retention, while the average Coulombic efficiency remains at 99.96%. The cell continues to operate stably for more than 4400 cycles. By contrast, the Zn||DC delivers a much lower discharge capacity of only 2.94 mAh cm^{-2} (58.57 mAh g^{-1}) and fails after approximately 1900 cycles. Compared with representative reported Zn–I_2 coin cells, GEL-DC exhibits a favorable combination of high areal capacity and long cycle life under high-compaction-density conditions (Figure 5b and Table S3), supporting the effectiveness of the implanted PAMPS-Zn hydrogel interphase.

An Ah-level Zn||GEL-DC pouch cell (10 cm × 10 cm) was also successfully fabricated (Figure S16), delivering an initial capacity of 1.15 Ah (190.5 mAh g^{-1}, 11.5 mAh cm^{-2}) at 1 C and retaining 87.5% of its capacity after 850 cycles, corresponding to an average capacity decay of only 0.0147% per cycle (Figures 5c, S16, and S17). Detailed cell parameters and the corresponding complete-cell energy-density calculation are provided in Table S2. Together with the literature data summarized for both coin-cell and pouch-cell configurations in Table S3, this pouch-cell design achieves a cell-level energy density of 22.7 Wh kg^{-1}, with further improvement potential by modifications in E/C and N/P ratios. Specifically, stable full-cell cycling is retained with 30 μm Zn foil in coin cells (N/P = 1.68) and 50 μm Zn foil in a 10 cm × 10 cm pouch cell (N/P = 2.73) (Figures S18 and S19). In addition, the Zn||GEL-DC pouch cell withstands a needle penetration test without thermal runaway, showing only transient voltage fluctuation and localized heating at the penetration site (Figure S20).

Importantly, the flexible GEL-DC electrode is also compatible with cylindrical-cell fabrication. As a proof-of-concept format demonstration, the flexible GEL-DC electrode was assembled into a standardized 14500 AA-type cylindrical cell (Figure 5d). A comparison with a commercial Ni-MH 14500 AA-type rechargeable battery shows similar discharge plateaus of approximately 1.2 V and comparable discharge-utilization regions (Figure 5e), demonstrating the compatibility of GEL-DC with the standardized cylindrical-cell format. Consequently, four self-fabricated Zn||GEL-DC cylindrical cells were connected in series to form a battery module, which successfully powered an electric toy car originally designed for a 4 V power supply. The module provided stable power output for more than 11 min of continuous operation (Figure 5f and Video S1), thereby demonstrating reliable operation under an external load. The precursor-solution infiltration and UV-induced in situ polymerization steps can be incorporated after roll-to-roll dry-electrode fabrication, providing proof-of-concept validation of process compatibility (Figure 5g) and highlighting its potential for practical manufacturing integration [17, 57].

3 | Conclusion

In summary, this work established the implanted PAMPS-Zn hydrogel interphase as an effective solution to the coupled kinetic and shuttle limitations of highly compacted dry-processed iodine cathodes. FTIR and Raman analyses verify the in situ formation of PAMPS-Zn, while SEM/EDS mapping, 3D-CT reconstruction, and TOF-SIMS depth profiling confirm its through-thickness penetration and the construction of a continuous Zn^{2+}-conducting network. DFT calculations and MD simulations reveal the dual role of fixed sulfonate sites in coordinating Zn^{2+} and repelling polyiodide anions, which is further supported by in situ EIS, GITT, rate-dependent CV, and in situ spectroscopic analyses. This dual regulation enables high iodine utilization, suppressed polyiodide migration, and improved reaction reversibility, delivering an areal capacity of 9.6 mAh cm^{-2} at 0.5 C and stable cycling over 4400 cycles at 5 C. Moreover, an Ah-level non-stacked pouch cell achieves an initial capacity of 1.15 Ah with 87.5% capacity retention after 850 cycles. These findings highlight implanted Zn^{2+}-conducting hydrogel networks as a promising strategy toward the development of high-areal-capacity aqueous Zn–I_2 batteries.

15213773, 2026, 42, Downloaded from https://onlinelibrary.wiley.com/doi/10.1002/anie.6865881 by Xiamen University, Wiley Online Library on [19/11/2026]. See the Terms and Conditions (https://onlinelibrary.wiley.com/terms-and-conditions) on Wiley Online Library for rules of use; OA articles are governed by the applicable Creative Commons License

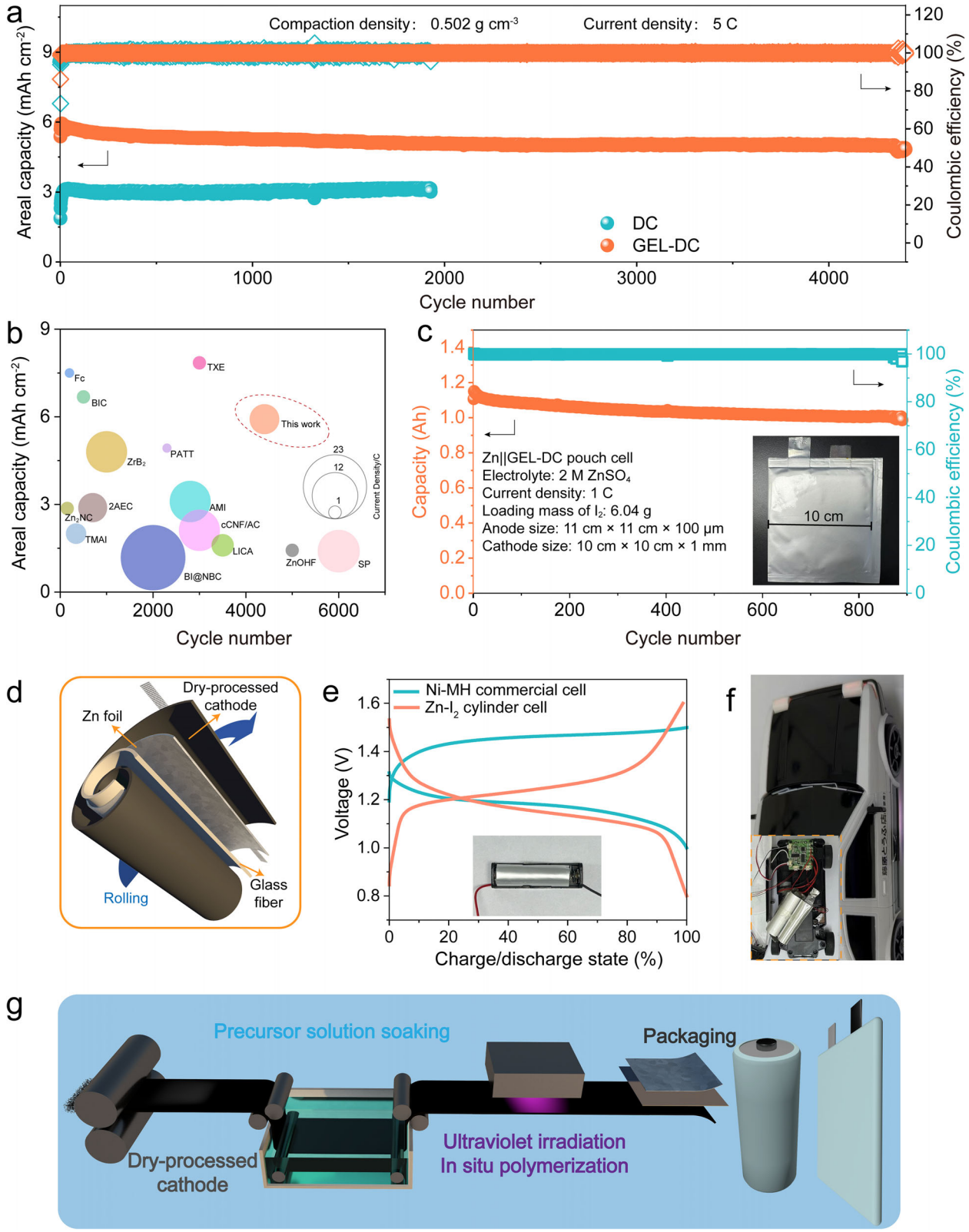

FIGURE 5 | Device-level proof-of-concept validation and fabrication compatibility. (a) Long-term cycling performance and Coulombic efficiency of coin cells based on DC and GEL-DC. (b) Performance comparison of representative reported aqueous Zn–I_2 coin cells in terms of areal capacity and cycling lifespan. (c) Cycling performance of an Ah-level pouch cell based on GEL-DC at 1 C, together with the corresponding photograph. (d) Schematic illustration of the custom cylindrical zinc-iodine battery in a standardized 14500 cylindrical format. (e) Charge-discharge curves of the zinc-iodine cylindrical battery in comparison with a commercial Ni-MH secondary battery, together with the photograph of the fabricated cylindrical cell. (f) Proof-of-concept demonstration of the cylindrical zinc-iodine battery module powering an electric toy car. (g) Schematic illustration of the manufacturing route, showing the compatibility of precursor infiltration, ultraviolet-induced in situ polymerization, and subsequent packaging with the dry-processing roll-to-roll production line.

15213773, 2026, 42, Downloaded from https://onlinelibrary.wiley.com/doi/10.1002/anie.6865881 by Xiamen University, Wiley Online Library on [19/11/2026]. See the Terms and Conditions (https://onlinelibrary.wiley.com/terms-and-conditions) on Wiley Online Library for rules of use; OA articles are governed by the applicable Creative Commons License

Author Contributions

Huadong Jiang: conceptualization, methodology, software, data curation, validation, formal analysis, investigation, visualization, writing – original draft. **Chenxi Sun:** methodology, software, data curation, writing – review and editing. **Hong Lin:** writing – review and editing, methodology, software, data curation. **Minghao Zhang:** methodology, writing – review and editing, validation, formal analysis, data curation, software, investigation. **Fanxiang Meng:** writing – review and editing, software, data curation. **Jinbao Zhao:** conceptualization, supervision, project administration, writing – review and editing, funding acquisition, resources. **Yang Yang:** funding acquisition, conceptualization, methodology, resources, supervision, writing – review and editing, project administration.

Acknowledgments

The authors gratefully acknowledge the financial support from National Natural Science Foundation of China (Nos. 22579141 and 22379125) and Fundamental Research Funds for the Central Universities (20720250114).

Conflicts of Interest

The authors declare no conflicts of interest.

Data Availability Statement

The data that support the findings of this study are available from the corresponding author upon reasonable request.

References

1. H. K. Bruce Dunn and J.-M. Tarascon, "Electrical Energy Storage for the Grid: A Battery of Choices," *Science* 334 (2011): 928–934, http://doi.org/10.1126/science.1212741.

2. A. Manthiram, "An Outlook on Lithium Ion Battery Technology," *ACS Central Science* 3 (2017): 1063–1069, https://doi.org/10.1021/acscentsci.7b00288.

3. N. Zhang, X. Chen, M. Yu, Z. Niu, F. Cheng, and J. Chen, "Materials Chemistry for Rechargeable Zinc-Ion Batteries," *Chemical Society Reviews* 49 (2020): 4203–4219, https://doi.org/10.1039/C9CS00349E.

4. D. Kundu, B. D. Adams, V. Duffort, S. H. Vajargah, and L. F. Nazar, "A High-Capacity and Long-Life Aqueous Rechargeable Zinc Battery Using a Metal Oxide Intercalation Cathode," *Nature Energy* 1 (2016): 16119, https://doi.org/10.1038/nenergy.2016.119.

5. X. Yu, Z. Li, X. Wu, et al., "Ten Concerns of Zn Metal Anode for Rechargeable Aqueous Zinc Batteries," *Joule* 7 (2023): 1145–1175, https://doi.org/10.1016/j.joule.2023.05.004.

6. D. Lin and Y. Li, "Recent Advances of Aqueous Rechargeable Zinc–Iodine Batteries: Challenges, Solutions, and Prospects," *Advanced Materials* 34 (2022): e2108856, https://doi.org/10.1002/adma.202108856.

7. S. J. Zhang, J. Hao, H. Li, et al., "Polyiodide Confinement by Starch Enables Shuttle-Free Zn–Iodine Batteries," *Advanced Materials* 34 (2022): e2201716, https://doi.org/10.1002/adma.202201716.

8. J. Xu, Z. Huang, H. Zhou, G. He, Y. Zhao, and H. Li, "Holistic Optimization Strategies for Advanced Aqueous Zinc Iodine Batteries," *Energy Storage Materials* 72 (2024): 103596, https://doi.org/10.1016/j.ensm.2024.103596.

9. H. Wen, H. Wen, Y. Sun, et al., "The Frontiers of Aqueous Zinc–Iodine Batteries: A Comprehensive Review on Mechanisms, Optimization, and Industrial Prospects," *Advanced Functional Materials* 35 (2025): 2500323, https://doi.org/10.1002/adfm.202500323.

10. J. L. Yang, M. Du, J. M. Cao, and X. L. Wu, "Sustainable Aqueous Zn-Ion Batteries: Green Materials, Low-Carbon Manufacturing, and Circular Economy," *Angewandte Chemie International Edition* 65 (2026): e7123448, https://doi.org/10.1002/anie.7123448.

11. M. Liu, Q. Chen, X. Cao, D. Tan, J. Ma, and J. Zhang, "Physicochemical Confinement Effect Enables High-Performing Zinc–Iodine Batteries," *Journal of the American Chemical Society* 144 (2022): 21683–21691, https://doi.org/10.1021/jacs.2c09445.

12. F. Wang, J. Tseng, Z. Liu, et al., "A Stimulus-Responsive Zinc–Iodine Battery With Smart Overcharge Self-Protection Function," *Advanced Materials* 32 (2020): e2000287, https://doi.org/10.1002/adma.202000287.

13. Y. Yang, S. Liang, B. Lu, and J. Zhou, "Eutectic Electrolyte Based on *N*-methylacetamide for Highly Reversible Zinc–Iodine Battery," *Energy & Environmental Science* 15 (2022): 1192–1200, https://doi.org/10.1039/D1EE03268B.

14. C. Li, R. Kingsbury, A. S. Thind, et al., "Enabling Selective Zinc-Ion Intercalation by a Eutectic Electrolyte for Practical Anodeless Zinc Batteries," *Nature Communications* 14 (2023): 3067, https://doi.org/10.1038/s41467-023-38460-2.

15. J. Ma, M. Liu, Y. He, and J. Zhang, "Iodine Redox Chemistry in Rechargeable Batteries," *Angewandte Chemie International Edition* 60 (2021): 12636–12647, https://doi.org/10.1002/anie.202009871.

16. H. Wu, J. Hao, S. Zhang, et al., "Aqueous Zinc–Iodine Pouch Cells With Long Cycling Life and Low Self-Discharge," *Journal of the American Chemical Society* 146 (2024): 16601–16608, https://doi.org/10.1021/jacs.4c03518.

17. J. Kim, K. Park, M. Kim, et al., "10 mAh cm^{-2} Cathode by Roll-to-Roll Process for Low Cost and High Energy Density Li-Ion Batteries," *Advanced Energy Materials* 14 (2024): 2303455, https://doi.org/10.1002/aenm.202303455.

18. J. H. Chang, M. W. Pin, I. Kim, et al., "Binder Migration: Frequently Observed yet Overlooked Phenomena in Electrode Processing for Lithium-ion Batteries," *Journal of Energy Storage* 83 (2024): 110729, https://doi.org/10.1016/j.est.2024.110729.

19. C. Zihrul, S. Wolf, and A. Kwade, "Model Experiments for Explaining the Processes Occurring During Conductive Battery Electrode Drying," *Energy Technology* 11 (2023): 2200671, https://doi.org/10.1002/ente.202200671.

20. Y. S. Zhang, N. E. Courtier, Z. Zhang, et al., "A Review of Lithium-Ion Battery Electrode Drying: Mechanisms and Metrology," *Advanced Energy Materials* 12 (2021): 2102233, https://doi.org/10.1002/aenm.202102233.

21. H. Wu, S.-J. Zhang, J. Vongsvivut, M. Jaroniec, J. Hao, and S.-Z. Qiao, "Aqueous Zinc-Iodine Batteries With Ultra-High Loading and Advanced Performance," *Joule* 9 (2025): 102000, https://doi.org/10.1016/j.joule.2025.102000.

22. H. Guo, H. Luo, F. Zhu, et al., "Mechanical-Thermal Decoupling Engineering Unlocks Ultra-Stable Dry Thick Iodine Cathodes for Ah-Level Zinc-Based Pouch Batteries," *Advanced Materials* 38 (2026): e73037, https://doi.org/10.1002/adma.73037.

23. C. Sun, M. Zhang, H. Xu, et al., "Scalable Roll-to-Roll Dry Processing of 10 mAh cm^{-2} Iodine Cathodes for Establishing Ah-Level Aqueous Zn–I_2 Pouch Cell Evaluation Protocol: Bridging Laboratory Research and Industrial Application," *Angewandte Chemie International Edition* 65 (2025): e17732, https://doi.org/10.1002/anie.202517732.

24. Y. Chen and S. Kong, "Advances and Challenges in Dry Electrode Process for Solid-State Batteries," *Journal of Solid State Electrochemistry* 30 (2026): 1441–1455, https://doi.org/10.1007/s10008-025-06518-4.

25. J. Yu, B. Kim, and Y. Yoo, "Dry Electrode Processing for Lithium-Ion Battery Cathodes and Anodes: Materials, Fabrication Strategies, and Future Outlook," *Advanced Materials Technologies* 10 (2025): e01420, https://doi.org/10.1002/admt.202501420.

26. R. Tao, B. Steinhoff, C. H. Sawicki, et al., "Unraveling the Impact of the Degree of Dry Mixing on Dry-Processed Lithium-Ion Battery Electrodes," *Journal of Power Sources* 580 (2023): 233379, https://doi.org/10.1016/j.jpowsour.2023.233379.

15213773, 2026, 42, Downloaded from https://onlinelibrary.wiley.com/doi/10.1002/anie.6865881 by Xiamen University, Wiley Online Library on [19/11/2026]. See the Terms and Conditions (https://onlinelibrary.wiley.com/terms-and-conditions) on Wiley Online Library for rules of use; OA articles are governed by the applicable Creative Commons License

27. A. Gyulai, W. Bauer, and H. Ehrenberg, "Dry Electrode Manufacturing in a Calender: The Role of Powder Premixing for Electrode Quality and Electrochemical Performance," *ACS Applied Energy Materials* 6 (2023): 5122–5134, https://doi.org/10.1021/acsaem.2c03755.

28. Y. Wang, J. Zhang, J. Xue, X. Ke, and G. Liang, "$LiFePO_4$/C Composites With High Compaction Density as Cathode Materials for Lithium-Ion Batteries With High Volumetric Energy Density," *Ionics* 27 (2021): 4687–4694, https://doi.org/10.1007/s11581-021-04078-x.

29. R. Zhu, G. Liu, G. Qu, et al., "Enhancing Volumetric Energy Density of $LiFePO_4$ Battery Using Liquid Metal as Conductive Agent," *Advanced Functional Materials* 34 (2024): 2409230, https://doi.org/10.1002/adfm.202409230.

30. S. Li, Y. Luo, K. Wang, L. Zhang, P. Yan, and M. Sui, "Opportunities and Challenges for Next-Generation Thick Cathodes in Lithium-Ion Batteries," *Materials* 18 (2025): 3464, https://doi.org/10.3390/ma18153464.

31. J. Wu, H. Guo, R. Wang, et al., "Fabrication of Low-Tortuosity Thick Electrodes With Low Material Loss by Temporally Shaped Ultraviolet Femtosecond Laser," *Nature Communications* 17 (2025): 973, https://doi.org/10.1038/s41467-025-67702-8.

32. A. V. Kubarkov, A. V. Babkin, O. A. Drozhzhin, K. J. Stevenson, E. V. Antipov, and V. G. Sergeyev, "Engendering High Energy Density $LiFePO_4$ Electrodes With Morphological and Compositional Tuning," *Nanomaterials* 13 (2023): 1771, https://doi.org/10.3390/nano13111771.

33. X. Yang, M. Xie, Z. Yan, et al., "High-Iodine-Loading Quasi-Solid-State Zinc–Iodine Batteries Enabled by a Continuous Ion-Transport Network," *Energy & Environmental Science* 18 (2025): 4730–4739, https://doi.org/10.1039/D5EE01170A.

34. M. Tang, Q. Liu, X. Zou, B. Zhang, and L. An, "High-Energy-Density Aqueous Zinc-Ion Batteries: Recent Progress, Design Strategies, Challenges, and Perspectives," *Advanced Materials* 37 (2025): e2501361, https://doi.org/10.1002/adma.202501361.

35. T. Xiao, J. L. Yang, B. Zhang, et al., "All-Round Ionic Liquids for Shuttle-Free Zinc-Iodine Battery," *Angewandte Chemie International Edition* 63 (2024): e202318470, https://doi.org/10.1002/anie.202318470.

36. J. L. Yang, Z. Yu, J. Wu, et al., "Hetero-Polyionic Hydrogels Enable Dendrites-Free Aqueous Zn-I_2 Batteries With Fast Kinetics," *Advanced Materials* 35 (2023): 2306531, https://doi.org/10.1002/adma.202306531.

37. J. H. Kang, W. Jeong, M. S. Kang, et al., "Multiscale Insights Enable Rational Design of Solvent-Free Dry Electrode Processing for Advanced Battery Electrode Fabrication," *Communications Materials* 7 (2025): 35, https://doi.org/10.1038/s43246-025-01046-0.

38. Z. Wen, Z. Hu, X. Wang, et al., "Weakening the Space Charge Layer Effect through Tethered Anion Electrolyte and Piezoelectric Effect Toward Ultra-Stable Zinc Anode," *Advanced Materials* 36 (2024): 2407390, https://doi.org/10.1002/adma.202407390.

39. J. Zheng, L. Wang, J. Xian, et al., "High-Loading Gel Cathodes Enabling Energetic Zinc Metal Batteries With Device-Level Capacities beyond 100 Ah L^{-1}," *Angewandte Chemie International Edition* 64 (2025): e21452, https://doi.org/10.1002/anie.202521452.

40. H. Song, J. Ma, J. Wan, X. Jia, and J. Liu, "A Janus Binder With Electrophilic and Nucleophilic Dual Centers for Ah-Level Four-Electron Aqueous Zn–I_2 Batteries," *Energy Storage Materials* 81 (2025): 104525, https://doi.org/10.1016/j.ensm.2025.104525.

41. Z. Chen, F. Wang, R. Ma, et al., "Molecular Catalysis Enables Fast Polyiodide Conversion for Exceptionally Long-Life Zinc–Iodine Batteries," *ACS Energy Letters* 9 (2024): 2858–2866, https://doi.org/10.1021/acsenergylett.4c00992.

42. Z. Zhu, D. Luo, L. Wei, et al., "Long-Life Aqueous Zinc–Iodine Batteries Enabled by Selective Adsorption of Polyiodide Anions in Nonporous Adaptive Organic Cages," *Energy Storage Materials* 75 (2025): 103994, https://doi.org/10.1016/j.ensm.2024.103994.

43. S. J. Zhang, J. Hao, H. Wu, Q. Chen, C. Ye, and S. Z. Qiao, "Protein Interfacial Gelation Toward Shuttle-Free and Dendrite-Free Zn–Iodine Batteries," *Advanced Materials* 36 (2024): e2404011, https://doi.org/10.1002/adma.202404011.

44. Q. Chen, J. Hao, Y. Zhu, et al., "Anti-Swelling Microporous Membrane for High-Capacity and Long-Life Zn—I_2 Batteries," *Angewandte Chemie International Edition* 64 (2024): e202413703, https://doi.org/10.1002/anie.202413703.

45. T. Liu, H. Wang, C. Lei, et al., "Recognition of the Catalytic Activities of Graphitic N for Zinc-Iodine Batteries," *Energy Storage Materials* 53 (2022): 544–551, https://doi.org/10.1016/j.ensm.2022.09.028.

46. J. Wu, J. L. Yang, B. Zhang, and H. J. Fan, "Immobilizing Polyiodides With Expanded Zn^{2+} Channels for High-Rate Practical Zinc-Iodine Battery," *Advanced Energy Materials* 14 (2023): 2302738, https://doi.org/10.1002/aenm.202302738.

47. X. Liao, Z. Zhu, Y. Liao, et al., "Cation Adsorption Engineering Enables Dual Stabilizations for Fast-Charging Zn—I_2 Batteries," *Advanced Energy Materials* 14 (2024): 2402306, https://doi.org/10.1002/aenm.202402306.

48. J.-H. Kim, N.-Y. Kim, Z. Ju, et al., "Upscaling High-Areal-Capacity Battery Electrodes," *Nature Energy* 10 (2025): 295–307, https://doi.org/10.1038/s41560-025-01720-0.

49. B. Nie, S. W. Lee, T. W. Wang, T. Liu, J. Li, and H. Sun, "Unveiling Multifunctional Synthetic Boundaries for Enhanced Mechanical and Electrochemical Performance in Densified Thick Composite Electrodes," *Nature Communications* 16 (2025): 9489, https://doi.org/10.1038/s41467-025-65257-2.

50. T. Weng, J. Guo, X. Li, et al., "Synthesis of the Polymerizable Room Temperature Ionic Liquid AMPS—TEA and Superabsorbency for Organic Liquids of Its Copolymeric Gels With Acrylamide," *Designed Monomers and Polymers* 17 (2013): 140–146, https://doi.org/10.1080/15685551.2013.840480.

51. J. Cong, X. Shen, Z. Wen, et al., "Ultra-Stable and Highly Reversible Aqueous Zinc Metal Anodes With High Preferred Orientation Deposition Achieved by a Polyanionic Hydrogel Electrolyte," *Energy Storage Materials* 35 (2021): 586–594, https://doi.org/10.1016/j.ensm.2020.11.041.

52. P. E. Blöchl, "Projector Augmented-Wave Method," *Physical Review B* 50 (1994): 17953–17979, https://doi.org/10.1103/PhysRevB.50.17953.

53. L. Ma, Y. Ying, S. Chen, et al., "Electrocatalytic Iodine Reduction Reaction Enabled by Aqueous Zinc-Iodine Battery With Improved Power and Energy Densities," *Angewandte Chemie International Edition* 60 (2021): 3791–3798, https://doi.org/10.1002/anie.202014447.

54. L. Zhao, D. Yin, Y. Zhang, et al., "Hydrophobic Ionic Liquid Enabled Polyiodide Confined Transport in a Cathode, Realizing High Areal Capacity, Stable Zinc–Iodine Batteries," *Energy & Environmental Science* 18 (2025): 8952–8963, https://doi.org/10.1039/D5EE02941D.

55. T. Liu, C. Lei, W. Yang, et al., "Solvent Chemistry Manipulated Iodine Redox Thermodynamics for Durable Iodine Batteries," *Angewandte Chemie International Edition* 64 (2025): e202422163, https://doi.org/10.1002/anie.202422163.

56. D. Yin, B. Li, L. Zhao, et al., "Polymeric Iodine Transport Layer Enabled High Areal Capacity Dual Plating Zinc-Iodine Battery," *Angewandte Chemie International Edition* 64 (2025): e202418069, https://doi.org/10.1002/anie.202418069.

57. W. Liu, H. Ma, L. Zhao, et al., "Anionically-Reinforced Nanocellulose Separator Enables Dual Suppression of Zinc Dendrites and Polyiodide Shuttle for Long-Cycle Zn–I_2 Batteries," *Nano-Micro Letters* 18 (2025): 59, https://doi.org/10.1007/s40820-025-01921-y.

Supporting Information

Additional supporting information can be found online in the Supporting Information section.

Supporting File 1: anie74221-sup-0001-SuppMat.docx.

Supporting File 2: anie74221-sup-0002-S1.mp4.

15213773, 2026, 42, Downloaded from https://onlinelibrary.wiley.com/doi/10.1002/anie.6865881 by Xiamen University, Wiley Online Library on [19/11/2026]. See the Terms and Conditions (https://onlinelibrary.wiley.com/terms-and-conditions) on Wiley Online Library for rules of use; OA articles are governed by the applicable Creative Commons License